FEDSM-ICNMM2010-30789

EXPERIMENTS ON AIR ENTRAINMENT DUE TO
FREE FALLING- AND WALL-JETS

Jose M. Lopez
The University of Tulsa
Tulsa, Oklahoma, USA

Dana V. Danciu
Forschungszentrum Dresden Rossendorf
Dresden, Saxony, Germany

Marco J. Da Silva
Forschungszentrum Dresden Rossendorf
Dresden, Saxony, Germany

Uwe Hampel
Forschungszentrum Dresden Rossendorf
Dresden, Saxony, Germany

Ram Mohan
The University of Tulsa
Tulsa, Oklahoma, USA

ABSTRACT

In this article, air entrainment as a result of an impinging round water jet and a wall-jet was experimentally studied by means of videometry and image processing methods and also by means of a measurement technique based on a wire-mesh sensor. Therefore, two different experimental setups were utilized. For the first setup, a series of experiments at different conditions was performed and evaluated for both round jets and wall-jets. Jet lengths ranged between 0.01 and 0.2 m and jet exit velocities between 0.9 and 3.5 m/s. Image processing algorithms were applied to extract information about jet penetration depth, width of the bubble plume and bubble size distribution. The second facility was used to create a falling film in a square pipe (5 cm x 5 cm). Downstream of the impact point, a wire-mesh sensor was used to measure the gas entrainment characteristics at one axial location. Video image processing was also used in this experiment to gather more qualitative information about the gas entrainment process. Video images are compared with the images obtained by the wire-mesh sensor showing good qualitative agreement. The induction trumpet and a thin sheet of gas that forms around the jet and penetrates into the pool causing the entrainment were clearly identified. Results indicate that the gas void fraction increases and the bubble size decreases as the superficial liquid velocity increases.

INTRODUCTION

The air entrainment occurs at the intersection of a water jet impinging the surface of a receiving pool. This process can be found in nature as waterfalls, breaking waves as well as in our daily life in a simple water fountain. The phenomenon of air entrainment is of importance in many industrial processes. Most relevant examples are found in nuclear engineering, crude oil extraction and processing, chemical process engineering and water aeration.

Impinging jets may occur during the cooling procedure in a loss of coolant accident (LOCA) in a pressurized water reactor (PWR). In the case of a LOCA, the integrity of the reactor pressure vessel (RPV) has to be maintained. In this scenario, cold water is injected into a PWR cold leg partially filled with hot water and steam, as discussed in [1]. Bubble entrainment, generated by the jet, influences the mixing of the hot and cold water. The mixing is important to limit thermal loads at the hot RPV walls. On the other hand, wall-jet impingement is very common in the oil transportation industry. Depending on the case, the entrainment process may be desirable or not. The falling film (wall-jet) impingement is typically encountered in the case of two-phase downward flow in vertical pipes, compact separators and downcomers [2], [3], [4]. In both applications, the correct control and prediction of the air entrainment process is essential for the efficiency and safe operation of systems.

Large and comprehensive studies about the entrainment caused by a jet impact on a liquid surface can be found in the

literature such as, computational simulation [5], experimental studies [1], [3], [6], [7], [8], , and modeling [1], [9], [10]. Despite all efforts made to understand and model this phenomenon there are many variables that affect the entrainment process that still need to be understood. In general, the entrainment phenomenon depends on the characteristics of the jet, nozzle, distance to the impingement point, and impact velocity, as described in [11]. However, further variables such as bubble penetration, gas void fraction, amount of gas entrained, and the entrainment mechanism itself need a more detailed investigation [4], [11], [12], [13].

Better understanding of the physics involved in the entrainment mechanism, bubble size distribution, amount of the entrained gas, and gas void fraction distribution in the liquid column, require innovative measurement techniques able to capture the dynamic complexity associated with each variable. Consequently, a combination of two different measurement techniques and two experimental setups are used in this study. A high-speed video camera is used in the first setup to gather qualitative information of the entrainment mechanism at the impact zone of the jet and the surface of the receiving pool. A novel and innovative measurement device, the wire-mesh sensor (WMS), is used in parallel with a high-speed video camera in the second setup. The WMS allows obtaining information about a series of important variables in the wall jet entrainment process, such as gas void fraction, gas void fraction distribution, bubble size distribution, and visualization of the bubble interaction of the two-phase flow phenomenon.

The WMS working principle is based on intrusive electrodes that collect data at high spatial and temporal resolution based on the resistant properties of the fluid [14], [15]. The WMS has been used by several researchers to experimentally study upward two-phase flow [14], [16], [17]. In this investigation, the WMS is used to study downward flow along with that reported by [3].

The main objectives of this experimental investigation are to gather more data on the gas entrainment mechanism and the parameters that play an important role in its occurrence. New data on the gas void fraction distribution, bubble size distribution, and flow visualization induced by the entrainment process was obtained by using the wire-mesh sensor technique. Additionally, images obtained with the WMS are compared with the images obtained from the high speed camera showing reasonable agreement in the case of the two-phase flow interaction images. Close observations of the induction trumpet and air meniscus were made, based on image processing analysis, revealing two different entrainment mechanisms for the flow conditions studied. Moreover, the penetration depth of the bubble plume was evaluated by means of image processing techniques showing a direct relationship with the jet velocity.

EXPERIMENTAL SETUP

For the study of the air entrainment phenomenon, two different measurement techniques and two different experimental setups were used:

- high-speed imaging for experiments carried out in a rectangular tank for jet impingement on a quiescent pool of water
- a wire-mesh sensor (WMS) used to study the downward movement of the bubbles in a rectangular pipe, for a falling film.

Impinging Jet Experiments

The round jet setup is schematically shown in Figure 1. The experiments were carried out in a 0.3 m x 0.3 m x 0.5 m water tank constructed with transparent acrylic walls for visualization purposes. Deionized water was pumped out of the tank and recirculated using a centrifugal pump. A rotameter was used for the measurement of the water flow rate. A smooth steel pipe of 6 mm inner diameter and 0.5 m length was used as a nozzle. The fluid properties of the deionized water correspond to 998 kg/m^3, 1.29x10^{-3} kg/m.s, and 5.05x10^{-2} N/m, for density, viscosity and surface tension, respectively.
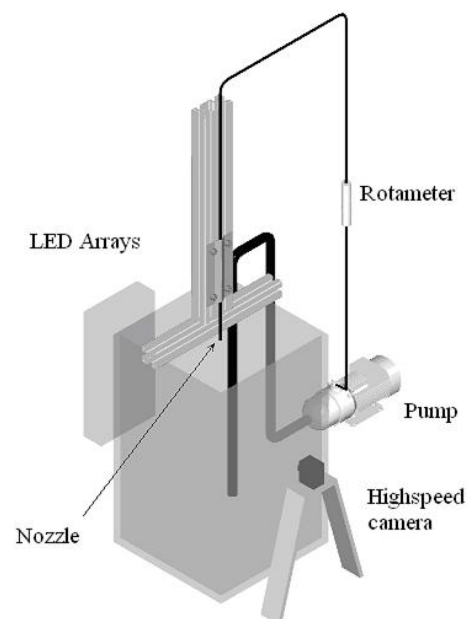

**Figure 1: Round Jet and Wall-jet Experimental Setup**

Images of the impact between the jet and the water pool were captured using a high-speed camera (DRS Technologies) in order to visualize the entrainment mechanism. The camera was operated with a frame rate of 1600 fps. Backlighting with high luminosity LED panels was used during the experiments in order to have a proper exposure at the required frame rate.

The experimental parameters consist of vertical liquid jet of different lengths and nozzle exit velocities impinging on the calm surface of the water pool at an angle of 90°. The nozzle was situated in the center of the cross-section of the tank to avoid the influence of the tank walls on the plume. The velocity of the jet ranged between 0.9 and 3.5 m/s at the nozzle exit and the jet length was varied between 0.01 and 0.2 m, keeping the water level in the tank constant.

Falling Film Impingement

The falling film experimental setup is described in detail in [3]. In general, the facility consists of a rectangular transparent

acrylic pipe of 0.05 m x 0.05 m cross-section and 2.0 m length, as shown in Figure 2.a. Rectangular pipe was chosen due to availability of the WMS geometry and simplicity of the data processing. The fluid used was deionized water. The falling film was created around a stagnant Taylor bubble, similar to the approach explained in [2]. The Taylor bubble was created at the upper end of the pipe by injecting air through a 3.0 mm tip needle. The water in the pipe flows downward around the Taylor bubble creating the falling film, as shown in Figure 2.b. The WMS was located at 1.30 m from the upper end of the pipe to measure the gas void fraction, gas void fraction distribution, and bubble size distribution. The superficial liquid velocities used in the experiments ranged from 0.18 to 1.46 m/s.
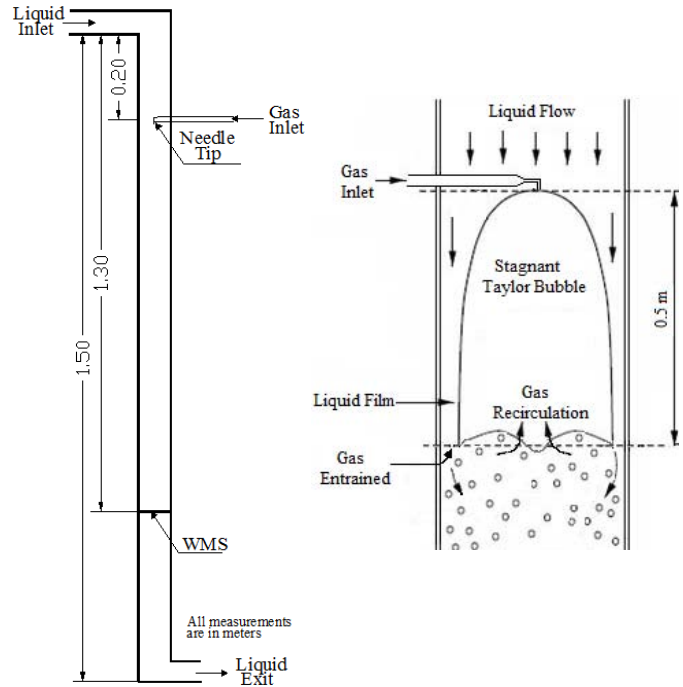
a. Schematic Facility   b. Schematic Stagnant Taylor Bubble

**Figure 2: Facility and Stagnant Taylor Bubble Schematic**

Wire-mesh sensor (WMS). The gas void fraction in the pipe was measured using a square WMS of 16x16 wires with 3 mm wire-separation operated by a capacitance-measuring electronics, as described in [3]. During the experiments, the WMS frequency was kept at 1600 fps. The WMS can acquire gas-liquid data with a 10% of uncertainty, as discussed by [14].

Additionally, videos were recorded using a high-speed camera. The camera was leveled perpendicular to the WMS measurement plane and parallel to the wall of the square pipe. The distance between the camera and the pipe was kept constant at 0.5 m. The videos were recorded at a frame rate of 1600 fps, which is also the WMS frame rate. Both, WMS and high-speed camera were triggered at the same time to ensure a direct comparison of the frames obtained from each device.

EXPERIMENTAL RESULTS

Impinging Jet
The characteristics of the jet are a key factor in the process of air entrainment [12], [18], [19], [20], [21]. During the experiments, the round jet was always, turbulent, with Reynolds numbers at the nozzle ranging $5000 \leq Re \leq 20000$. It was found that for all tested velocities, the surface of the jet was rough with bulk fluid traveling along it. Even at velocities for which no air entrainment occurred this characteristic was observed. Figure 3 shows the tendency of the jet surface for three different nozzle exit velocities.
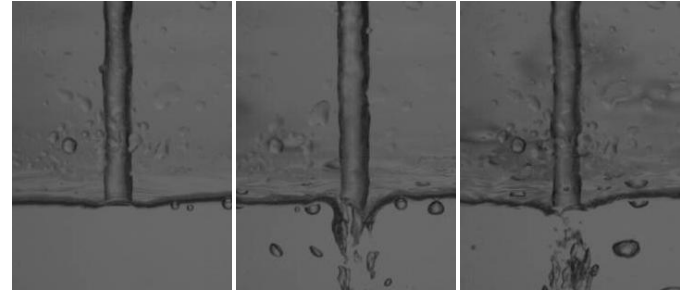
a. $v_0 = 1.48$ m/s   b. $v_0 = 1.67$ m/s   c. $v_0 = 1.96$ m/s

Figure 3: Round Jet Characteristics for Three Different Velocities

Two different entrainment mechanisms were observed for the entire test matrix. The first entrainment mechanism was observed for low velocity turbulent jets (vj ≤ 2 m/s) and occurs due to the disturbances that travel along the jet surface [10]. In this case the surface of the pool cannot follow the jet undulations and the entrainment process occurs. The entrainment caused by this type of jet behavior is pulsating. Big air pockets are being entrained each time a wave on the jet surface impacts the receiving pool. The pockets are dragged downwards and broken into smaller bubbles by the turbulent forces. Due to the energy dissipation in the plume, some of the bubbles start coalescing and escape from the diffusion cone, moving first sideways and then upwards. A recirculation zone is created around the diffusion cone by the upward moving bubbles. The liquid surface surrounding the jet is bubbly and foamy as a result of the rising bubbles. The irregularity of the liquid pool surface is another factor that contributes to the entrainment process.   Figure 4 shows the entrainment process caused by such a jet surface disturbance.
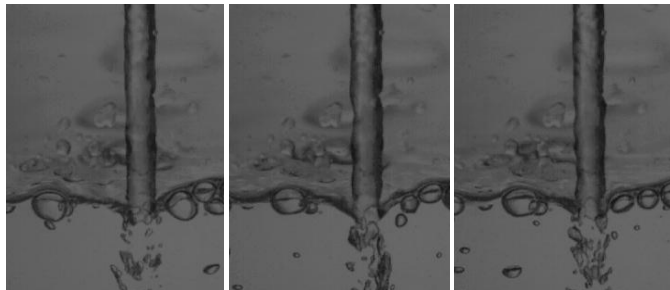
The second entrainment mechanism is due to the depression of the liquid surface surrounding the jet at the impact point and was observed for turbulent jets with velocities higher than 2 m/s [20]. At this point, an air meniscus forms around the jet at the plunging point and penetrates the liquid pool. As the meniscus moves downward, it becomes unstable and the jet of water begins to break through the bottom of the meniscus, tearing down bubbles from the air layer. Figure 5 shows the entrainment mechanism.   Figure 4 and Figure 5 are showing for first time in the literature real pictures of the entrainment mechanism. These figures are valuable for further references in the investigation of the entrainment process.
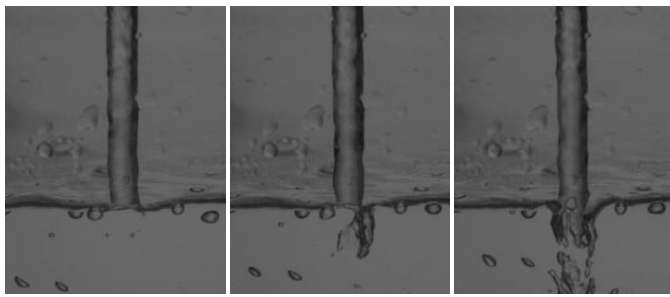
a. Before contact   b. At contact   c. After contact
(t = 0 ms)   (t = 5.6 ms)   (t = 12.5 ms)

Figure 4: Round Jet Gas Entrainment Process.
$v_0 = 1.67$ m/s

a.   t = 0 ms   b.   t = 26.8 ms   c.   t = 42.5 ms

Figure 5: Example of the Second Entrainment
**Mechanism. $v_0 = 1.96$ m/s**

It was observed during the experiments that by varying the jet length at a constant nozzle velocity, the jet diameter at the impact point and the momentum transfer from the jet into the pool change. Therefore, if the jet length is increased keeping the nozzle velocity constant, the jet diameter decreases, but the momentum transfer from the jet into the pool increases. Some other aspects also may contribute to non-monotonous entrainment behavior. Surface instabilities caused by the turbulence inside the jet or triggered by the edge of the nozzle may be damped with increasing jet length.

Falling Film Impingement in a Square Pipe
As it was described earlier, a square facility was used to carry out wall-jet experiments around a stagnant Taylor bubble, as shown in Figure 2. The entrainment process of the wall-jet is similar to the entrainment process described for the round-jet. As mentioned in [2], waves play an important role in the entrainment mechanism for the wall-jets. That becomes more evident when the surface of the receiving pool is wavy and the wall-jet is thicker and wavy enough. Also, when the wall-jet velocity is high enough a change in the mechanism occurs and the meniscus penetrating the pool dominates the entrainment process [19].

For all experimental conditions tested in the square pipe, it was observed that the surface of the wall-jet and the surface of the liquid at the impact point were wavy, as shown in Figure 6a. Due to the high amount of air being entrained and to the highly wavy and turbulent surface of the receiving liquid, a clear observation of the entrainment mechanism during the experiments was not possible, even though a high-speed camera was used. One phenomenon could still be clearly observed: The movement of the bubbles close to the impact point shows that in the center of the pipe a column of rising bubbles was formed, while close to the wall a column of downward moving bubbles was observed. A schematic is shown in Figure 6.b.
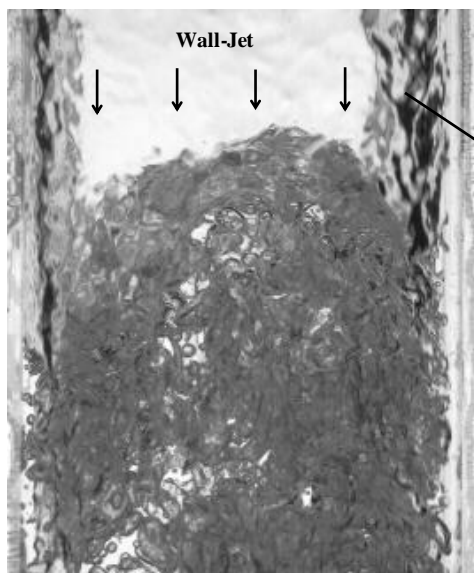
a. Photo of waves on receiving
pool and on wall-jet surface
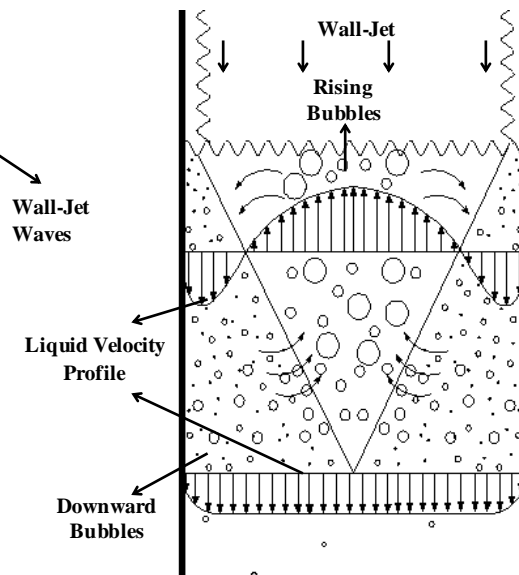
b. Schematic of bubble
column movement

Figure 6: Waves and Bubble Movements

The main focus of this experiment was the characterization of the gas entrained downstream of the rear of the Taylor bubble. The WMS is an intrusive measurement technique which can disturb the bubbles movement. The WMS has been previously used only for upward pipe flow measurements, because in upward flow the drag forces and buoyancy forces follow the

same direction, reducing the WMS intrusive effect. For downward flow, buoyancy and drag forces are opposed and the WMS intrusive effect can play an important role when these two forces are close in magnitude. During the experiments, the intrusive effect of the WMS was clearly observed for a superficial liquid velocity range of 0.19 to 0.53 m/s. For the lowest velocity (0.19 m/s), big air pockets were formed at the lower plane of the WMS. Those bubbles moved randomly, changing shape but never crossing the lower plane of the WMS nor breaking. This is shown in the sequence of pictures in Figure 7. For a velocity of 0.53 m/s such big air pockets do not occur anymore. However, at that velocity, bubbles are being observed to be moving randomly upward and downward between the WMS-wires, crossing the wires several times and being measured several times. That leads to a gas void fraction value that is higher than the value resulted from the developed bubbly flow in which the bubbles pass through the WMS and are measured only one time. For the superficial liquid velocity range of 0.6 to 1.45 m/s the bubbles are always moving downward and never pass through the wires more than one time (developed flow).
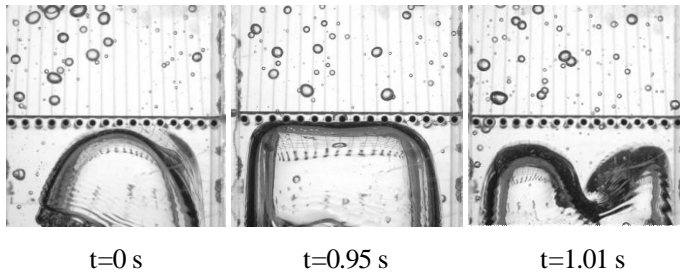

| t=0 s | t=0.95 s | t=1.01 s |

Figure 7: Bubble Formation at the Lower WMS Measurement plane Vsl=0.19 m/s

Image processing algorithms were used in order to qualitatively characterize the bubble size distribution and the spatial bubbles distribution in the square pipe from the WMS raw experimental data. The image reconstruction algorithms are explained in [3], [14], [16], [17]. Additionally, high-speed videos were taken during the experiments. A qualitative comparison between data from the high-speed camera and the image reconstruction of the WMS data is shown in Figure 8.

In the WMS image reconstruction, the red color represents 100% air while the blue color represents 100% water. It is important to note in Figure 8 that the WMS shows the void fraction distribution in the cross-section while the high-speed camera image is a lateral image of the pipe. Images are presented in pairs, WMS and high-speed camera, so that comparison can be made. Small bubbles can be located easily in each pair of figures. The comparison between the WMS images and the high speed video cameras images evidence one of the capabilities of the WMS. Flow images of the cross section of the flow are key parameters to understand the bubble interaction and movements [3].
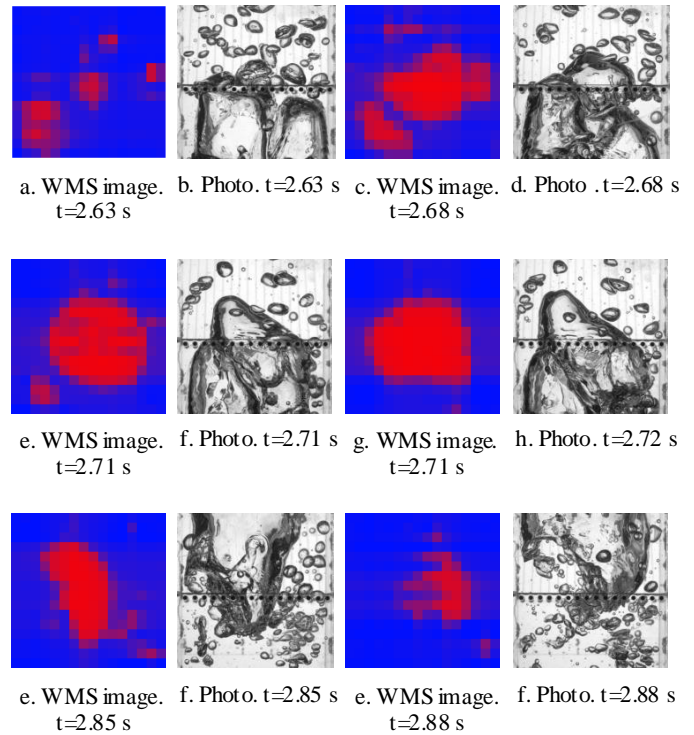

a. WMS image. t=2.63 s	b. Photo. t=2.63 s	c. WMS image. t=2.68 s	d. Photo. t=2.68 s
e. WMS image. t=2.71 s	f. Photo. t=2.71 s	g. WMS image. t=2.71 s	h. Photo. t=2.72 s
e. WMS image. t=2.85 s	f. Photo. t=2.85 s	e. WMS image. t=2.88 s	f. Photo. t=2.88 s

Figure 8: High-speed Camera and WMS Images Comparison in Wall-jet Square Test Facility. v = 0.28 m/s

Capabilities of the WMS are beyond image reconstruction of the two-phase flow. Further quantitative analysis of the data obtained from the WMS can be performed, such as instantaneous gas void fraction, gas void fraction distributions over the pipe cross section, and gas void fraction time traces. The signals obtained from each crossing point in the mesh are stored in the form of a tridimensional matrix $\alpha_{i,j,k}$, where k represent the time index, and i, j are the indices for the spatial location of the measurement point, as shown in Figure 9.
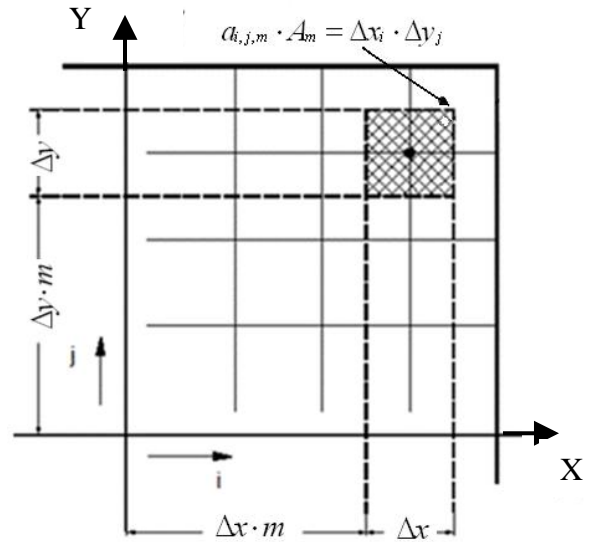

Figure 9: Crossing Points Identification

The local gas void fraction stored in the matrix $\alpha_{i,j,k}$ can be averaged in time and/or any of the two spatial directions, to obtain different gas void fraction profiles. In order to perform this, the averaging weight coefficients $(a_{i,j})$ are defined. These coefficients represent the contribution of each crossing point (i,j) to the area of the entire control volume (m) to be studied. Usually weight coefficients that are in the center of the sensor have the same value. However, crossing point of the WMS that are close to wall not always contribute with their complete sensing area $(\Delta x, \Delta y)$ because of the pipe wall interfere. In such cases, the weight coefficients of those crossing points will have a lower value, meaning that it has lower contribution to the averaging process. Figure 9 shows the control volume (m) of area (A_m) and sensing area defined by $(\Delta x, \Delta y)$.

The spatial average time trace can be carried out by adding the contribution of each measurement point for both spatial locations (i, j) of the tridimensional matrix. This average will lead to matrix that contains the average spatial gas void fraction as a function of time. Such operation can be expressed mathematically according to Eq. 1. Figure 10 shows the spatial average time trace for one superficial liquid velocity.

$$\overline{\alpha}_k = \alpha(t) = \sum_i \sum_j a_{i,j} \cdot \alpha_{i,j,k} \qquad (1)$$

An average gas void fraction for the total cross-sectional area can be calculated averaging the gas void fraction matrix over the time and over the spatial directions i and j, as presented in Eq. 2.

$$\overline{\alpha} = \sum_i \sum_j a_{i,j} \cdot \overline{\alpha}_{i,j} = \frac{1}{k_{max}} \sum_{k=1}^{k_{max}} \overline{\alpha}_k \qquad (2)$$
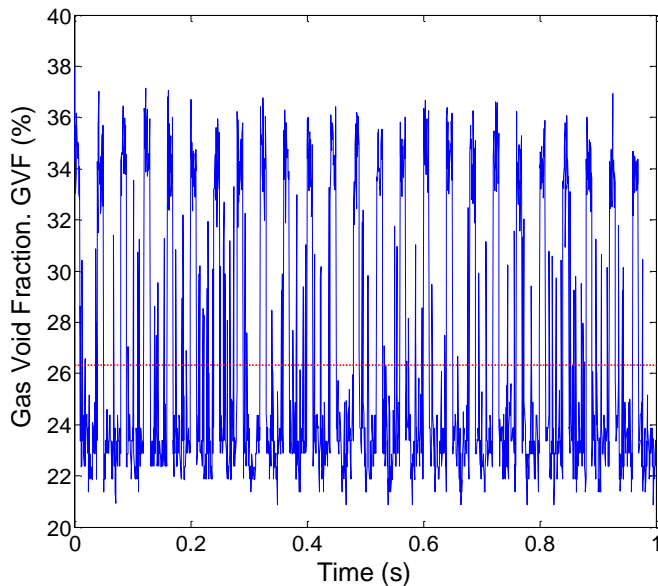

Figure 10: Spatial Average Time Trace Gas Void Fraction. Vsl=1.47 m/s

A summary of the total average gas void fraction for all experimental conditions is given in Figure 11. The general trend observed in Figure 11 shows that the gas void fraction increases as the superficial liquid velocity increases. Basically, three different variables, namely, the wall-jet impact velocity, the drag force, and the bubble size distribution are playing an important role in the mechanism that controls the amount of air carried under. Increasing liquid flow rate results in an increment of the wall-jet impact velocity. Consequently, the gas entrainment rate increases as the wall-jet impact velocity increases. Additionally, the drag force increases as the superficial liquid velocity increases. Therefore, bigger bubbles can be dragged downwards with the liquid which increases the amount of gas carried under. Furthermore, the turbulence level increases as the superficial liquid velocity increases. Consequently, turbulence forces can break down the bubbles generated in the entrainment process, creating smaller bubbles dispersed in the liquid column. The smaller the bubble diameter is, the smaller the buoyancy force will be. Buoyancy force is opposed in direction to the drag force, so it is easier for the drag force to carry down a bubble to the liquid exit. In general, the combination of these variables results in an increment of the gas void fraction as shown in Figure 11.
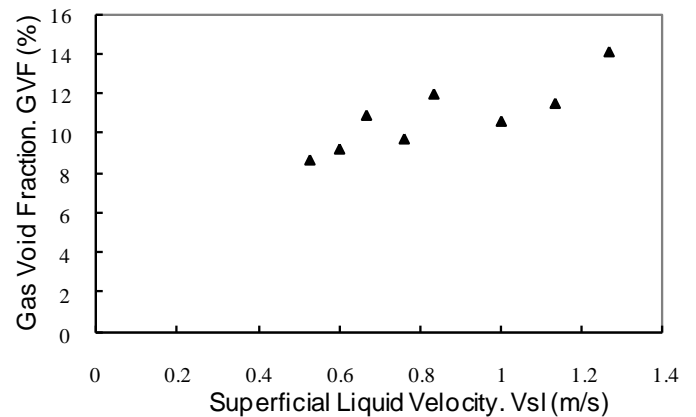

Figure 11: Time Averaged Gas Void Fraction

Furthermore, the transversal gas void fraction across the square pipe can be calculated. This represents the variation of the average gas void fraction from the center of the pipe to the wall.
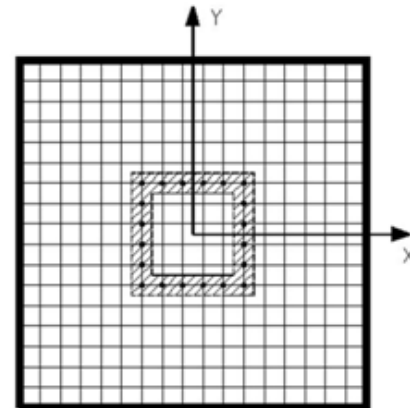

Figure 12: Transversal Gas Void Fraction Control Volumes

The void fraction is calculated by performing an averaging operation over time (k) and spatially (i,j) over the differential

areas or control volumes, as shown in Figure 12. Equation 3 describes the way this average is being calculated.

$$\overline{\alpha}_m = \frac{1}{k_{max}} \sum_k \sum_i \sum_j a_{i,j,m} \cdot \alpha_{i,j,k} \qquad (3)$$
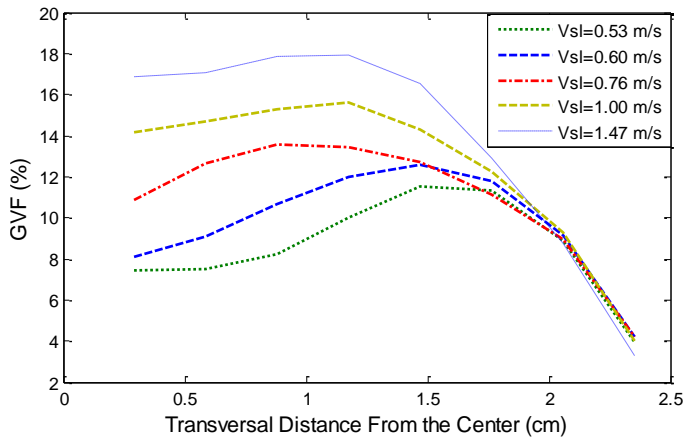

Figure 13: Transversal Gas Void Fraction Profiles

The transversal gas void fraction is plotted in Figure 13 as function of the superficial liquid velocity. Each curve represents the variation of the gas void fraction as the transversal distance increases. The transversal distance is measured from the center of the pipe up to the wall. It can be observed that for low superficial liquid velocities the maximum gas void fraction is not towards the center. This indicates that the flow field is probably not developed at the axial distance where the measurements were taken. It is shown in Figure 6 that, for the non developed velocity profiles of the submerged wall-jet, more gas is observed in the flow field towards the wall. As the superficial liquid velocity increases, the diffusion cone diameter increases. Once the diameter of the diffusion cone is big enough, all bubbles show a downward velocity profile. Such profile is characterized to have a flat front towards the center of the pipe. This description seems to be coherent with the transversal gas void fraction profile of 1.47 m/s. This behavior is in agreement with the results presented in Figure 11.

Another important analysis that can be made from the WMS data is quantifying the contribution of the different bubble sizes to the total gas void fraction. Therefore, the gas void fraction profiles per bubble class can be calculated using the information recorded with the WMS. The process of bubbles size classification is explained in [17]. Basically, the bubbles are classified and grouped according to the diameter. Afterwards, spatial average of the gas void fraction per class can be performed during the entire period of measurements. An example of the results for the gas void fraction per bubble class is shown in Figure 14. It can be observed how different bubble classes are contributing to the total gas void fraction. Bubble class with diameters less than 4 mm can be seen during the entire period of measurement. However, the contribution of these bubbles to the total gas void fraction is not significant. On the other hand, bubble class with diameters between 4 and 7 mm, have more contribution to the total gas void fraction than the bubble class with diameters smaller than 4 mm. Sometimes, this bubble class represents almost the total gas void fraction, as can be seen in the periods of time 0.40-0.41, 0.43-0.45, and 0.51-0.53. Bubble classes with diameters between 7 to 10 mm and 10 to 33.5 mm appear with a lower frequency than the bubble classes with diameters less than 4 mm and 4 to 7 mm. However, when those big bubbles pass through the WMS, the contribution to the total gas void fraction is significant, especially for the case of bubble class with bubble diameters between 10 to 33.5 mm.
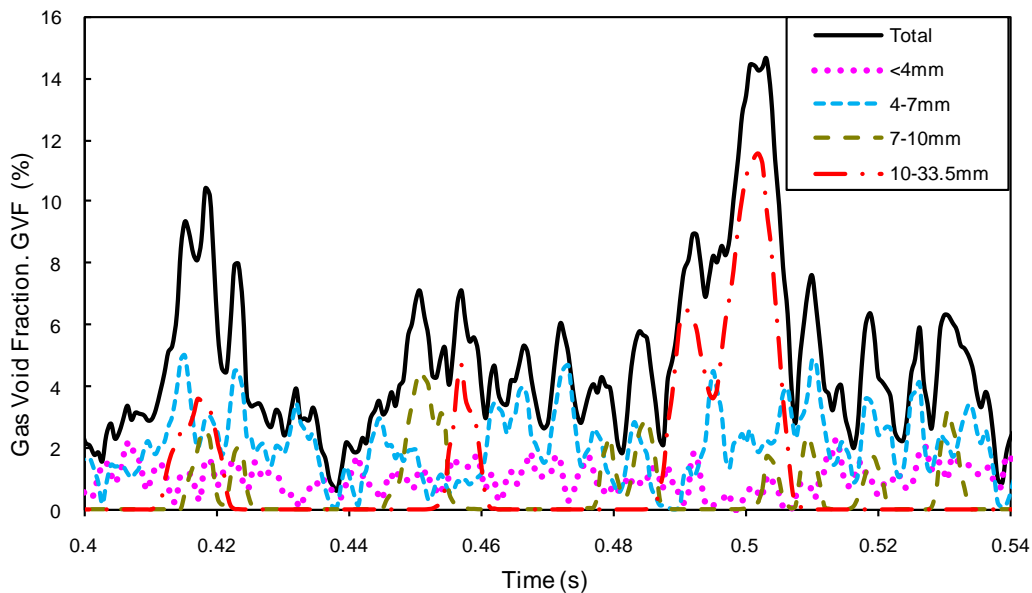

Figure 14: Gas Void Fraction Time Series per Bubble Class. Vsl=1.1 m/s

CONCLUSIONS

Two different facilities were used to successfully study the entrainment process for round jet and wall jet. Visual observations, image processing techniques and local measurements using the wire-mesh sensor allowed the acquisition of valuable information about the entrainment process, flow visualization, gas void fraction, and bubble distribution below the impact point.

Very important observations on the entrainment mechanism of a round jet were made. The result of the analysis of the pictures from the high speed camera clearly demonstrates the physical phenomenon of the entrainment process. Basically, two different entrainment mechanisms were identified for the entire test matrix. The first entrainment mechanism occurs due to the disturbances that travel along the jet surface, causing a pulsating entrainment process. The second mechanism is due to the air meniscus that is formed around the jet at the plunging point and penetrates the liquid pool. Instabilities and turbulence forces tear down bubbles from the air layer, causing gas entrainment. This second entrainment process is more continuous than the first one.

Additionally, in the wall-jet case high-speed video camera allowed recording the movement of the bubbles close to the impact point. The bubbles exhibited a typical profile of a column of rising bubbles in the center and a column of downward moving bubbles close to the wall. Despite the high resolution of the camera, clear observations of the mechanism of entrainment were not possible due to the highly aerated flow, the wavy surface of the film and the receiving pool.

The WMS was successfully used to measure the gas void fraction distribution, bubble size distribution, total gas void fraction, and as a flow visualization tool. It was possible to obtain visual information of the cross sectional plane of the pipe by analyzing the images obtained from the WMS. The intrusive effect of the WMS was observed to be negligible for superficial liquid velocities higher than 0.6 m/s. Below this velocity, the intrusive effect of the WMS caused a bubble concentration in the lower plane of the sensor. Good agreement between the high-speed camera and the image reconstruction of the WMS was obtained. Next step of investigation may include round pipes in order to eliminate possible effects of the corners on the flow field.

ACKNOWLEDGMENT

NOMENCLATURE

a	Weight coefficient
d	Diameter
H	Height
k	Time array index
L	Length
v	Velocity

Sub and Super Index

i	Direction (x direction) or array rows
j	Direction (y direction) or array columns
k	Direction (time direction) or tridimensional array index
max	Maximum
P	Penetration
o	Initial
N	Nozzle
J	Impact

Greek Symbols

α	Gas void fraction
$\bar{\alpha}$	Average gas void fraction

REFERENCES

[1] Lucas, D., Bestion, D., Bodèle, E., Coste, P., Scheuerer, M., D'Auria, F., Mazzini, D., Smith, B., Tiselj, I., Martin, A., Lakehal, D., Seynhaeve, J.-M. , Kyrki-Rajamäki, R., Ilvonen, M., and Macek, J., 2008, "An Overview of the Pressurized Thermal Shock Issue in the Context of the NURESIM Project", Science and Technology of Nuclear Installations, Vol. 2009, pp. 1-13.

[2] Kockx, J.P., Nieuwstadt, F.T.M., Oliemans, R.V.A., and Delfos, R., 2005, "Gas Entrainment by a Liquid Film Falling Around a Stationary Taylor Bubble in a Vertical Tube," Int. Journal of Multiphase Flow, Vol. 31, pp. 1-24.

[3] Lopez, J. M., Danciu, D. V., Da Silva, M. J., Hampel, U., Mohan, R., 2010, "Experimental Study and Flow Visualization of Gas Entrainment in Downward Flow," Proceedings of the 7th . International Conference on Multiphase Flow, ICMF2010, Tampa, USA.

[4] Ohkawa, A., Kusabiraki, D., Kawai, Y., and Sakai, N., 1986, "Some Flow Characteristics of a Vertical Liquid Jet System Having Downcomers," Chemical Engineering Science, Vol. 41, pp. 2347-2361.

[5] Schmidtke, M., and Lucas, D., 2009, "CFD Approaches for Modeling Bubble Entrainment by an Impinging Jet," Science and Technology of Nuclear Installations, Vol. 2009, Article ID 148436, 12 pages, 2009.

[6] Bonetto, F., and Lahey, Jr. R.T., 1993, "An Experimental Study on Air Carryunder Due to a

Plunging Liquid Jet," Int. J. Multiphase Flow, Vol. 19, No. 2, pp. 281-294.

[7] Chanson, H., and Brattberg, T., 1997, "Experimental Investigations of Air Bubble Entrainment in Developing Shear Layers," Univ. of Queensland, Dep. of Civil Eng., Report CH48/97.

[8] Cummings, P. D., and Chanson, H., 1999, "An Experimental Study of Individual Air Bubble Entrainment at a Planar Plunging Jet," Trans. I. Ch. E., Vol. 76, pp. 159-164.

[9] Chanson, H., Aoki S., and Hoque, A., 2004, "Physical Modeling and Similitude of Air Bubble Entrainment at Vertical Circular Plunging Jets," Chem. Eng. Sci., Vol. 59, pp. 747-758.

[10] Cummings, P. D., and Chanson, H., 1997, "Air Entrainment in the Developing Region of Plunging Jets-Part 1," Journal of Fluids Engineering, Vol. 119, pp. 597-602.

[11] Mckeogh, E. J., and Ervine D.A., 1981, "Air Entrainment Rate and Diffusion Pattern of Plunging Liquid Jets," Chemical Engineering Science, Vol. 36, pp. 1161-1172.

[12] Mckeogh, E. J., 1978, "A Study of Air Entrainment Using Plunging Water Jets," Ph.D. Thesis, Queen's University of Belfast, UK, 374 pages.

[13] Sene, K. J., 1988, "Air Entrainment by Plunging Jets," Chemical Engineering Science, Vol. 43, pp. 2615-2623.

[14] Da Silva, M. J., Schleicher, E., and Hampel, U.,2007, "Capacitance Wire-Mesh Sensor for Fast Measurement of Phase Fraction Distributions,". Measurement Science and Technology, Vol. 18, pp. 2245-2251.

[15] Prasser, H.-M., Böttger, A., Zschau, J., 1998, "A New Electrode-Mesh Tomograph for Gas-Liquid Flows," Flow measurement and instrumentation, Vol. 9, pp. 111-119.

[16] Da Silva, M. J., 2008, "Impedance Sensors for Fast Multiphase Flow Measurement and Imaging, " Ph.D. Dissertation, Technische Universität Dresden, Germany, 154 pages.

[17] Prasser, H.-M., Scholz, D., and Zippe, C., 2001, "Bubble Size Measurement Using Wire-Mesh Sensor," Flow measurement and instrumentation, Vol. 12, pp. 299-312.

[18] Bin, A. K., 1993, "Gas Entrainment by Plunging Liquid Jets". Chem. Eng. Science, Vol. 48, No. 21, pp. 3585-3630.

[19] Lin, T. J., and Donnelly, H. G., 1966, "Gas Bubble Entrainment by Plunging Laminar Liquid Jets," A. I. Ch. E. Journal, Vol.12, pp. 563-571.

[20] Van de Donk, J., 1981, "Water Aeration with Plunging Jets," Ph.D. Thesis, TU Delft, The Netherlands, 168 pages.

[21] Van de Sande, E., and Smith John, M., 1973, "Surface Entrainment of Air by High Velocity Water Jets," Chemical Engineering Science, Vol. 28, pp. 1161-1168.